

Force Balance Model for Bubble Rise, Impact, and Bounce from Solid Surfaces

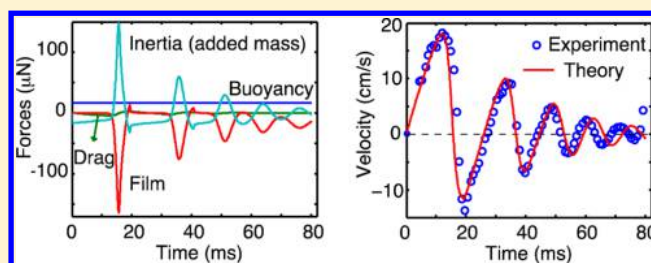
Rogério Manica,^{*,†} Evert Klaseboer,[†] and Derek Y. C. Chan^{‡,§}

[†]Institute of High Performance Computing, 1 Fusionopolis Way, Singapore 138632, Singapore

[‡]School of Mathematics and Statistics, The University of Melbourne, Victoria 3010, Australia

[§]Department of Chemistry and Biotechnology, Swinburne University of Technology, Hawthorn 3122, Australia

ABSTRACT: A force balance model for the rise and impact of air bubbles in a liquid against rigid horizontal surfaces that takes into account effects of buoyancy and hydrodynamic drag forces, bubble deformation, inertia of the fluid via an added mass force, and a film force between the bubble and the rigid surface is proposed. Numerical solution of the governing equations for the position and velocity of the center of mass of the bubbles is compared against experimental data taken with ultraclean water. The boundary condition at the air–water interface is taken to be stress free, which is consistent for bubbles in clean water systems. Features that are compared include bubble terminal velocity, bubbles accelerating from rest to terminal speed, and bubbles impacting and bouncing off different solid surfaces for bubbles that have already or are yet to attain terminal speed. Excellent agreement between theory and experiments indicates that the forces included in the model constitute the main physical ingredients to describe the bouncing phenomenon.



INTRODUCTION

The rise and impact of bubbles against a solid surface is a fundamental problem in many industrial applications that has received considerable attention both experimentally^{1–4} and theoretically.^{5–8} For small (radius, $R < 60 \mu\text{m}$) spherical bubbles rising under Stokes flow that neglect the effect of fluid inertia in the limit of zero Reynolds number, analytical solutions were obtained^{9,10} for mobile and immobile hydrodynamic boundary conditions on the bubble surface. Bubbles in water in the Stokes flow regime remain spherical and start to slow down at a distance many bubble radii away from the surface, and such bubbles will approach and settle on the surface without bouncing. These theoretical predictions agree with experimental data^{11,12} provided the effects of surface forces such as van der Waals and repulsive electrical double layer are also included at submicrometer separations.

For large bubbles traveling at high velocities and hence high Reynolds number due to large buoyancy force, the effect of inertia can no longer be neglected. Such bubbles will also exhibit considerable deformations both during rise and especially during impact with the surface. Furthermore, such bubbles can bounce a few times before finally adhering or settling close to the solid surface.¹ Surprisingly, even bubbles in water impacting on a horizontal air/water interface bounce before bursting into upper air phase.^{13,14}

The boundary condition that needs to be applied at the air–water interface depends on the cleanliness of the system. In the presence of impurities or added surfactants, the boundary condition at the bubble surface can shift from tangentially mobile to partially mobile or fully immobile depending on the

concentration of impurities or added surfactants.^{15–17} Consequently, the terminal velocity of bubbles at high Reynolds numbers can vary by about a factor of 2 between clean^{18,19} and contaminated bubbles,^{2,3} whereas in the low-speed Stokes flow regime²⁰ (i.e., small size bubbles) the difference is only a factor of 3/2. Early experiments on bubble terminal velocity were probably prone to contamination, as can be seen from the large variations in terminal speed in a compilation of data from various authors.²¹

Full numerical solution of the Navier–Stokes equations have been performed for bubbles rising and impacting on surfaces using the volume of fluid method⁸ that is capable of reproducing the consecutive bounces as observed in experiments.¹ The major challenge is in predicting accurately the shape of the draining fluid film between the bubble and the rigid surface whose thickness is orders of magnitude smaller than the size of the bubble. This requires the use of refined grids that increases significantly the computational cost.

On the other hand, lubrication theory is very accurate when the separation between the bubble and the surface becomes smaller than other dimensions. It has proven successful in comparison with a number of experimental data from the literature, summarized in recent reviews^{22,23} or, for example, in Taylor bubble modeling.²⁴ In those systems the deformable interfaces were driven at low speeds, and the entire system was under the Stokes flow regime.

Received: April 24, 2015

Revised: May 29, 2015

Published: June 2, 2015

Recent improvements in high-speed photography allow measurements of bubble position and thin film drainage at relatively high impact velocities using synchronized cameras.³ The experiments were modeled by using the experimental bubble velocity as a boundary condition to the drainage equations, and the numerical solutions showed the utility of lubrication in capturing the drainage phase accurately.^{25,26} Recently, a model that uses the bubble velocity based on a force balance as the boundary condition to the drainage equations was proposed for spherical bubbles with tangentially immobile condition at the bubble surface.⁵ This model was successful in predicting trajectories as well as thin film drainage compared with the experimental data³ in a contaminated system. Bubbles in clean water systems exhibit a much more pronounced bouncing behavior than contaminated bubbles due to their greater impact speed. Experiments concerning bubbles in clean systems appear to be remarkably reproducible,¹ and proper modeling of inertial effects is now of utmost importance.

Given the availability of recent well-controlled experimental data and our improved theoretical understanding, it is timely to revisit and extend the force balance model for mobile and deformable bubbles at even higher Reynolds numbers. The model is inspired by early work⁶ that takes into account the deformation of the bubble during rise²⁷ and incorporates modifications of the added mass effect due to the presence of the rigid surface.²⁸ It is applicable for bubbles that follow a vertical straight path, so that the system remains axisymmetric during the impact and drainage processes.

We assume the dynamics of the bubble can be modeled using an equation of motion of a “point particle”

$$\Sigma F = F_A + F_B + F_D + F_F = ma \approx 0 \quad (1)$$

where F_A is the added mass force, F_B the buoyancy force, F_D the drag force, and F_F the film force due to the lubrication pressure build up in the film between the deformed bubble and the surface. Inertia effects of the fluid comprise a history force that is negligible for clean bubbles at high Reynolds numbers²⁹ and an added mass force that varies with separation between the bubble and the rigid surface. Although the mass of the bubble m can be ignored, the inertia effect of the fluid that arises from the acceleration a of the bubble needs to be taken into account. We will discuss each force individually. The results of the proposed model will be compared with experimental data from the literature for bubbles that rise from rest, bubbles at terminal velocity, and bubbles impacting solid horizontal surfaces.

■ TERMINAL SPEED: BALANCE BETWEEN BUOYANCY AND DRAG

In order to model the correct behavior of a bouncing bubble, it is crucial to obtain the correct terminal velocity when it is far from the surface. This is found by balancing the buoyancy and drag force taking into account deformation of the rising bubble. If the deformation is overestimated for a given equivalent radius, the cross-sectional area of the bubble will be too large, resulting in more drag and hence a lower terminal velocity. In this section, the relation between the buoyancy force, drag force, and deformation will be investigated.

In Figure 1 we introduce the parameters that are needed for the development of the model. A bubble of equivalent radius R rises with velocity $V(t)$ before impacting a horizontal solid surface (t is time). Depending on the size and velocity, the bubble can attain an oblate ellipsoid shape during rise as

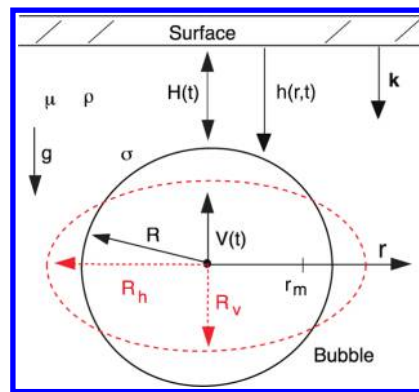


Figure 1. Schematic of the experimental system: An air bubble with equivalent radius R and interfacial tension σ rises with velocity $V(t)$ in clean water with zero tangential stress boundary condition (t indicates time) with viscosity μ and density ρ . Dashed line corresponds to the shape of the ellipsoidal bubble.

indicated by the dashed shape. The equivalent radius R is defined as

$$R = \left(\frac{3V_o}{4\pi} \right)^{1/3} \quad (2)$$

where the volume V_o of the bubble is given by $V_o = (4\pi/3)R_h^2R_v$ with R_h being the horizontal radius and R_v the vertical radius of the ellipsoidal bubble. The aspect ratio of the deformed bubble is defined as $\chi = R_h/R_v$. In the experiments of Duineveld¹⁸ a bubble rising with terminal velocity with $R = 0.5, 0.75,$ and 1.0 mm gives $\chi \approx 1.1, 1.5,$ and 2.0 , respectively. On the basis of these results, the deformation of the bubble needs to be taken into account if $R > 0.3$ mm.

A bubble rising in a liquid experiences a buoyancy force, which is equal to the density of the fluid ρ , multiplied by the gravitational constant, g , and the volume of the bubble

$$F_B = -\rho g \frac{4}{3} \pi R^3 \mathbf{k} \quad (3)$$

The density of the gas inside the bubble has been neglected. The unit vector \mathbf{k} points in the vertical direction of gravity g .

When a bubble moves in a liquid, it experiences a drag force of the form²⁷

$$F_D = C_D \text{Re} \frac{\pi}{4} \mu R V \mathbf{k} \quad (4)$$

where $\text{Re} = 2R\rho V/\mu$ is the instantaneous Reynolds number. For a bubble rising at terminal velocity V_T , the velocity is simply $V = V_T$. The drag coefficient C_D was calculated analytically for an ellipsoidal bubble with zero tangential stress boundary condition²⁷ and has the form

$$C_D \text{Re} = 48G(\chi) \left(1 + \frac{K(\chi)}{\sqrt{\text{Re}}} \right) \quad (5)$$

with $\chi = R_h/R_v$ and

$$G(\chi) = \frac{1}{3} \chi^{4/3} (\chi^2 - 1)^{3/2} \frac{[\sqrt{\chi^2 - 1} - (2 - \chi^2)s^{-1}(\chi)]}{[\chi^2 s^{-1}(\chi) - \sqrt{\chi^2 - 1}]^2} \quad (6)$$

The function K was found numerically²⁷ and can be approximated by the following polynomial⁶

$$K(\chi) = 0.0195\chi^4 - 0.2134\chi^3 + 1.7026\chi^2 - 2.1461\chi - 1.5732 \quad (7)$$

At steady state, terminal velocity is determined by $F_B + F_D = 0$. The bubble will then rise at a constant speed V_T that depends on the aspect ratio χ .

It was observed by Duineveld¹⁸ that if the experimental aspect ratio is provided in the model of Moore²⁷ then the predicted terminal velocity using Moore's analytical expression for C_D corresponds to the experimentally observed terminal velocity. Therefore, an expression for the aspect ratio as a function of equivalent radius is desired. We can find an approximated expression for the aspect ratio using a ratio between polynomials (see Figure 2a) that best fits the experimental data. The expression for the inverse aspect ratio is then written as

$$\chi^{-1} = \frac{0.74 + 0.45\lambda}{1 - 1.17\lambda + 2.74\lambda^2} \quad (8)$$

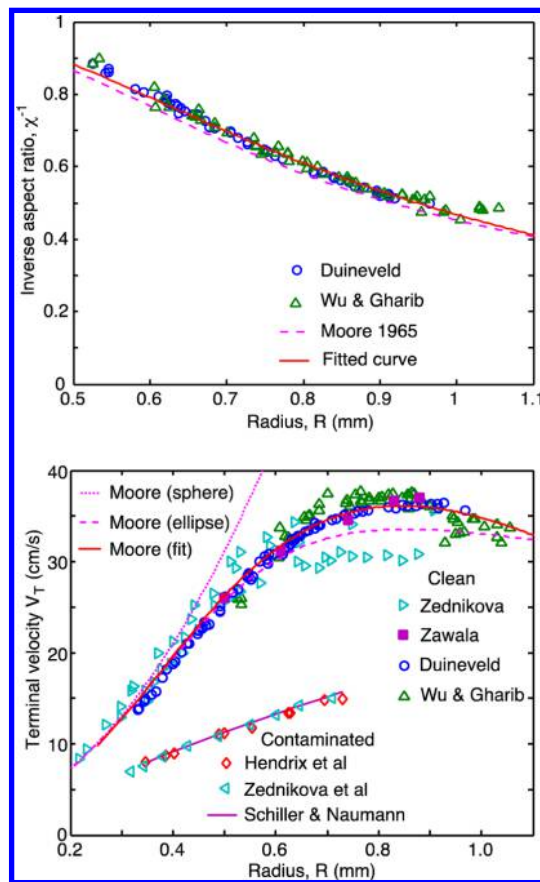


Figure 2. (a) Inverse aspect ratio χ^{-1} of rising bubbles in clean water. The continuous line corresponding to using eq 5 and the dashed line corresponding to Moore²⁷ calculation are compared with experiments of Duineveld¹⁸ and Wu and Gharib.¹⁹ (b) Terminal velocity of bubbles rising in bulk. (Top cluster) Bubbles rising in clean water systems from various experimental sources^{1,13,18,19} are compared with the theory of Moore²⁷ assuming a spherical (dotted), ellipsoidal (dashed), and ellipsoidal with eq 8 for the aspect ratio fit (solid line). The Reynolds number ranges between 50 and 700. (Bottom cluster) Bubbles rising in surfactant systems^{2,3} remain mostly spherical, and their terminal velocity is compared with the empirical relation for solid spheres with no slip boundary condition of Schiller and Naumann.³¹

where $\lambda = R/R_0$ and $R_0 = 1$ mm that is accurate for $0.3 \text{ mm} < R < 1 \text{ mm}$ or equivalently $0.3 < \lambda < 1$. The constants were chosen to give the best fit to the experimental data. For $R < 0.3 \text{ mm}$ the deformation is negligible and a spherical shape can be assumed, and for $R \gtrsim 1 \text{ mm}$ the bubble starts to zigzag and movement is no longer in a straight path.¹⁸

The curve of the inverse aspect ratio given by eq 8 is also shown in Figure 2a. It was designed to fit the experimental data of Duineveld¹⁸ and Wu and Gharib.¹⁹ Moore's result overestimates the deformation (dashed line) slightly, and this will result in a noticeable effect on the terminal velocity.

The terminal velocity V_T as a function of radius of rising bubbles is shown in Figure 2b. Experimental data^{1,13,18,19} of rising bubbles in a clean water system are compared with the analytical solution for ellipsoidal bubbles given by Moore²⁷ and also using the aforementioned fit for the aspect ratio of eq 8 in Moore's drag force (eqs 4–7). The combination of the analytical result of Moore and our fit for the aspect ratio are used to predict the terminal velocity of such bubbles. Note that if the bubble would remain spherical, the terminal velocity would continue to increase as a function of the radius, but with deformation included the velocity has a maximum at $R \approx 0.8 \text{ mm}$ before it decreases.

Analytical expressions for the aspect ratio as a function of equivalent bubble radius that are valid for small deformations were given by Moore²⁷ as $\chi = 1 + 9We/64$ and also by Legendre et al.³⁰ as $\chi = 1/(1 - 9We/64)$. In these expressions the Weber number, $We = 2R\rho V^2/\sigma$, is required, which is a function of velocity.

The terminal velocity for bubbles in contaminated systems is lower by about a factor of 2 when compared to clean systems. The experimental data of Zednikova et al.² and Hendrix et al.³ agree well with the empirical drag relation for solid spheres with no slip boundary condition proposed by Schiller and Naumann³¹ where the drag coefficient is given empirically by

$$C_D Re = 24(1 + 0.15Re^{0.687})$$

ACCELERATING BUBBLES: THE ADDED MASS FORCE

Now that we have seen how the terminal velocity can be obtained, we will extend the theory toward a bubble accelerating from rest. Besides the bubble itself, part of the surrounding fluid must also be accelerated. This will give rise to the added mass force. First, consider a bubble accelerating from rest in a liquid far away from any boundary. The added mass force inertial effect is given by

$$\frac{4}{3}\pi R^3(\rho C_m + \rho_b)\frac{dV}{dt}\mathbf{k} \quad (9)$$

where C_m is the added mass coefficient. For a spherical bubble in an infinite domain, $C_m = 1/2$, while for an oblate ellipsoidal bubble C_m depends on the bubble's aspect ratio.⁶ Since we are dealing with bubbles in water, the density of the air contents of the bubble ρ_b is much smaller than the density of the surrounding liquid, ρ , and can thus be neglected. Balancing the forces of eqs 3, 4, and 9 results in a differential equation for an accelerating bubble as

$$\frac{4}{3}\pi R^3\rho C_m\frac{dV}{dt} = \frac{4}{3}\pi R^3\rho g - C_D Re\frac{\pi}{4}\mu RV \quad (10)$$

In Figure 3 we compare the theoretical result of eq 10 for the position and velocity of the bubble as a function of time with

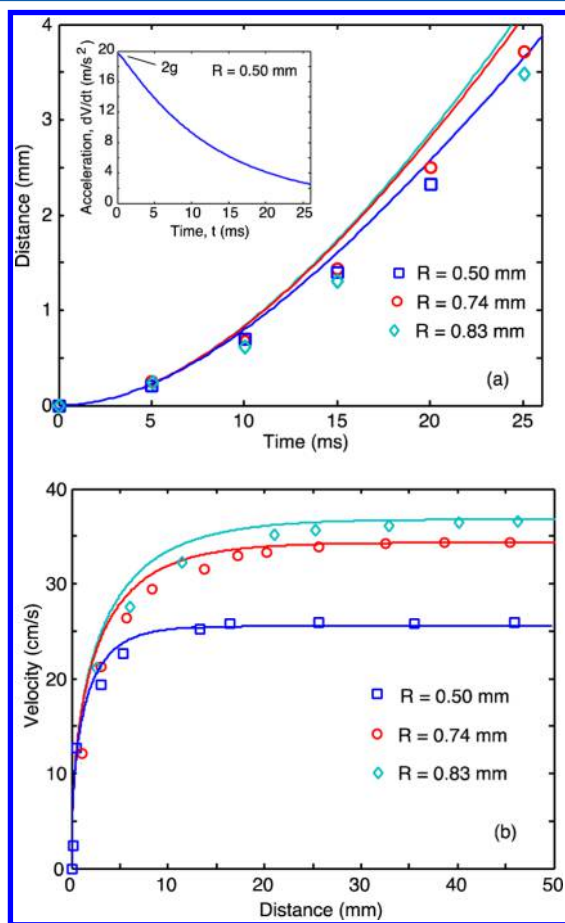


Figure 3. Comparison between theory (lines) and experiments of Zawala and Malysa¹³ (symbols) for bubbles with different radii. (a) Distance as a function of time, where the inset shows the acceleration for the bubble with $R = 0.5$ mm. (b) Velocity as a function of distance traveled.

the experimental data of Zawala and Malysa.¹³ The bubbles with different radii are released from a syringe from rest ($V = 0$ at $t = 0$) and accelerate. Theoretically we assume the aspect ratio given by eq 8 for the deformation, which will provide the same deformation as a bubble at constant terminal velocity. We have taken $C_m = 1/2$ for the added mass coefficient, which is the case for the start of the acceleration process when the bubbles are still spherical. When the bubbles become deformed, the assumption of a spherical bubble underestimates the added mass effect, and consequently, the bubbles travel faster than those of the experiment. For the smaller bubble with $R = 0.50$ mm, the agreement is reasonable as the deformation remains small. In reality, both the aspect ratio χ and the added mass coefficient C_m are functions of the velocity (and thus of time), but for simplicity we have taken them as constants ($C_m = 1/2$ and χ given by eq 8).

In Figure 3a we see that experimentally the distance traveled by bubbles of different radii in the first 25 ms after release from rest is very similar. This is because larger bubbles deform significantly and the extra drag caused by the larger projected area compensates for the buoyancy increase. The inset shows the evolution of the acceleration of the bubble, which is $2g$ initially because $C_m = 1/2$ in eq 10. However, as the drag effect

increases, the acceleration decreases to zero when the bubble reaches terminal velocity. In Figure 3b we show that the model captures the bubble acceleration phase as well as the terminal velocity. We notice that the bubble reaches about 90% of its constant terminal velocity after traveling just over 10 radii. The terminal velocity is then determined by the balance between buoyancy and drag force, as shown in the previous section.

The next step in the formulation is to obtain an expression for the added mass for a bubble that is impacting on a surface. This will be done using an energy approach based on potential flow theory.²⁸ The kinetic energy E_K of the system is defined as

$$E_K = \frac{1}{2} V^2 \frac{4}{3} \pi R^3 C_m \rho \quad (11)$$

where we have again neglected the density of the bubble. The power applied to the system can be described by

$$-V \mathbf{F}_A = -\frac{dE_K}{dt} \mathbf{k} = -\rho \frac{4}{3} \pi R^3 \left(C_m V \frac{dV}{dt} + \frac{1}{2} V^2 \frac{dC_m}{dH} \frac{dH}{dt} \right) \mathbf{k} \quad (12)$$

C_m is no longer a constant but depends on the separation between the bubble and the surface, H , with $dC_m/dt = (dC_m/dH)(dH/dt)$. In our model H is taken to be the film thickness between the bubble and the surface at the axis of symmetry (Figure 1) even if deformation is present. For a spherical bubble approaching a surface,^{28,32} the force can be written as (noting that $dH/dt = -V$)

$$\mathbf{F}_A = \left(\rho \frac{4}{3} \pi R^3 C_m \frac{dV}{dt} - \frac{1}{2} \rho \frac{4}{3} \pi R^3 \frac{dC_m}{dH} V^2 \right) \mathbf{k} \quad (13)$$

The first term on the right-hand side of this equation represents the classical added mass force (eq 9), and it depends on the acceleration of the bubble. The second term arises from the fact that the added mass coefficient C_m changes when the bubble approaches the surface.²⁸ The second term is proportional to V^2 and thus always points in the direction away from the surface irrespective of whether the bubble is moving toward or away from the surface. This also implies that it does not contribute to the damping of the system.

The added mass coefficient C_m for a sphere approaching a solid wall is approximated as²⁸

$$C_m = \frac{1}{2} + 0.19222\zeta^{-3.019} + 0.06214\zeta^{-8.331} + 0.0348\zeta^{-24.65} + 0.0139\zeta^{-120.7} \quad (14)$$

where $\zeta = (H + R)/R$ (see Figure 1). For a sphere in bulk $C_m = 1/2$.

■ LUBRICATION THEORY AND DEFORMATION: FILM DRAINAGE FORCE

The final yet essential piece of the model consists of two components: a lubricating film between the bubble and the surface combined with surface tension which will govern the deformation of the bubble in this area. This balance between viscous lubrication and deformation of the bubble will give rise to a pressure build up in the film great enough to cause rebound.

The film drainage force, which is calculated from the area integral of the pressure in the film, assuming axisymmetric film drainage

$$\mathbf{F}_F = \left(\int p \, dA \right) \mathbf{k} = \left(\int_0^\infty 2\pi r p \, dr \right) \mathbf{k} \approx \left(\int_0^{r_m} 2\pi r p \, dr \right) \mathbf{k} \quad (15)$$

where r_m is the size of the computational domain of the lubrication theory and the pressure in the film p is calculated from the classical film drainage Stokes–Reynolds equation²² in axial symmetric form for a mobile bubble surface and immobile solid surface, that is, the velocity is zero at the solid surface and the shear stress is zero at the bubble surface

$$\frac{\partial h}{\partial t} = \frac{1}{3\mu r} \frac{\partial}{\partial r} \left(r h^3 \frac{\partial p}{\partial r} \right) \quad (16)$$

The pressure p in the film obeys the Young–Laplace equation of the form²²

$$p = \frac{2\sigma}{R} - \frac{\sigma}{r} \frac{\partial}{\partial r} \left(r \frac{\partial h}{\partial r} \right) \quad (17)$$

Equation 17 is crucial for the model, since the surface tension is the only component capable of storing energy due to deformation. During rebound, the energy stored in the pressure build up (even when $V = 0$) is given back to the bubble as kinetic energy. In our calculations the disjoining pressure Π is neglected since it is only important at separations below ~ 100 nm just before rupture of the film and we are mostly interested in the bouncing behavior of the bubble which happens at film thicknesses $> 1 \mu\text{m}$.

To solve the drainage eqs 16 and 17 we require one initial and four boundary conditions. The initial condition assumes a parabolic profile based on the equivalent radius R of the bubble: $h(0, r) = H_0 + r^2/(2R)$ with $H_0 = H(t = 0)$. This will automatically create a zero pressure profile at $t = 0$ in eq 17. The axial symmetric domain is discretized from $0 < r < r_m$, where r_m is comparable to the radius R of the bubble ($r_m = 0.9R$). Symmetry conditions for p and h are imposed at the center of symmetry ($r = 0$). At the far field boundary ($r = r_m$) we assume the pressure vanishes ($p \approx 0$) and impose the velocity of the center of mass V based on the force balance model through a boundary condition of the form $dh/dt = -V$ at $r = r_m$. The time evolution of the velocity V of the bubble is calculated by balancing all forces (eqs 3, 4, 13, and 15) resulting in the following evolution equation

$$\frac{4}{3} \pi R^3 \rho C_m \frac{dV}{dt} = \frac{4}{3} \pi R^3 \rho g - C_D \text{Re} \frac{\pi}{4} \mu R V + \frac{2}{3} \pi R^3 \rho \frac{dC_m}{dH} V^2 - \int_0^{r_m} 2\pi r p \, dr \quad (18)$$

Equation 18 is solved to determine the value of V that is used as the boundary condition at $r = r_m$ for dh/dt , which drives the system according to the drainage eq 16. It is added as an extra equation to the linear evolution system (after finite difference in the spatial derivatives), which is solved using *ode15s* in Matlab. Here, C_m is a function of separation (eq 14), so is dC_m/dH . The instantaneous Reynolds number Re is calculated at each time step based on the velocity V , and $C_D \text{Re}$ is given by eq 5. The pressure p is calculated from eq 17.

This completes the theoretical formulation for the impact of clean bubbles with surfaces. In the next section we compare the theoretical results of eqs 16–18 with experimental data available.

SOME EXPERIMENTAL OBSERVATIONS

Before we can apply the theoretical model described in the previous sections to predict bubble bounces during impact with a solid surface in clean water systems we investigate a number of experiments performed for bubbles rising under buoyancy after being released from rest from a syringe in a water container.^{1–4,13,14} Let's first investigate the experimental data of Kosior et al.¹ in which different experimental aspects were considered: bubbles released far or near a solid surface or air–water interface, bubbles impacting on different solid surfaces, and bubbles in the presence of added surfactants or in different alcohols. In Figure 4 we reproduce typical experimental data in

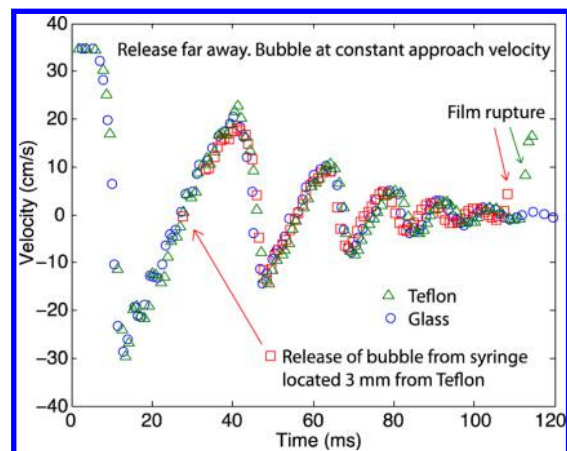


Figure 4. Experimental data from Kosior et al.¹ for the velocity of several bubbles in clean water (all $R = 0.74$ mm) that were released from a syringe at a great distance (triangle and circle) or at a distance of 3 mm (square) and impacting different solid surfaces (Teflon or glass). Positive velocity represents approach and negative velocity rebound. Experimental data for the bubble that was released from 3 mm was shifted by about 25 ms such that all data points overlap.

clean water for two bubbles of the same size ($R = 0.74$ mm) impacting on different surfaces¹ released far from the surface and one released from a syringe 3 mm from the surface. Experimental results show that these bubbles bounce in a very reproducible way, while film rupture depends strongly on the nature of the surface. For example, collisions with hydrophobic Teflon result in bubble rupture due to surface roughness, whereas rupture did not occur in collisions with smooth glass surfaces.

Figure 4 indicates that releasing the bubble at 3 mm from the surface is very similar to releasing the bubble far away but starting from the second bounce. Our theoretical model will be compared with some typical experimental data.

BUBBLE RELEASE NEAR THE SURFACE

We start our modeling by studying the case where the bubble was released from a syringe 3 mm away from a Teflon plate. Comparison between theory and experiment¹ is shown in Figure 5a. The radius of the bubble is $R = 0.74$ mm, and therefore, $H_0 = 1.52$ mm is the initial separation between the bubble and the surface. The bubble accelerates and impacts the surface long before reaching terminal velocity (35 cm/s), so we can neglect deformation during rise ($\chi = 1$). The domain size was taken to be $r_m = 0.9R$ as in a previous study.⁵ The bubble bounces a few times before adhering to the surface at time 80 ms when the experimental rupture of the film occurred. The

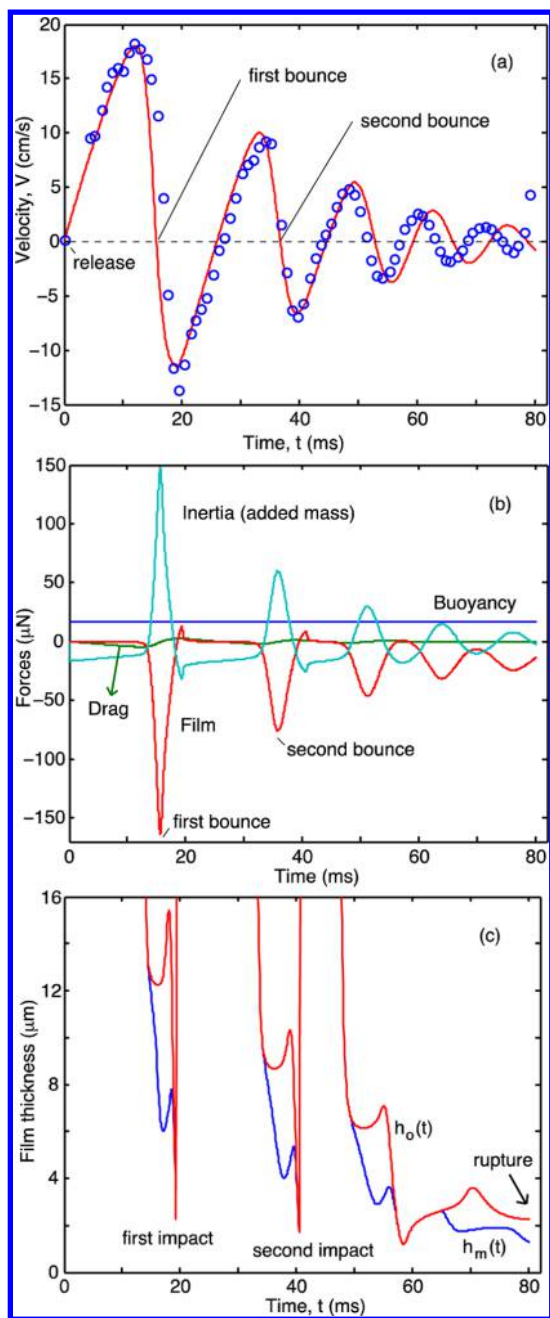


Figure 5. Bubble of radius $R = 0.74$ mm is released from a syringe located 3 mm away from a Teflon surface. (a) Experimental bubble velocity¹ (circles) is compared with the model proposed by eqs 16–18 (line). Theoretical domain size is taken as $r_m = 0.9R$, and the bubble was assumed to have a spherical shape ($\chi = 1$). (b) Evolution of forces during multiple impacts. Buoyancy is constant throughout the process, while drag is small. Film force and added mass are large and have opposite effects. Note the film force changes sign during the pull-off phase. (c) Film thickness at the center h_o and at the rim h_m (as defined in Figure 6). Note the similarity of the first and second impacts.

model is able to predict the subsequent bounces of the bubble, only slightly deviating toward the end.

The evolution of forces on a bubble released 3 mm from the surface during consecutive bounces is shown in Figure 5b. The major contributions to the bouncing process come from the balance between added mass and film force. Even though the drag force is very small in comparison with the balance between

added mass and film force, it is still necessary to be included to capture the experimental bounces accurately.

In Figure 5c we show the film thickness at the center of the film h_o (see Figure 6a) and at the rim h_m of the bubble where

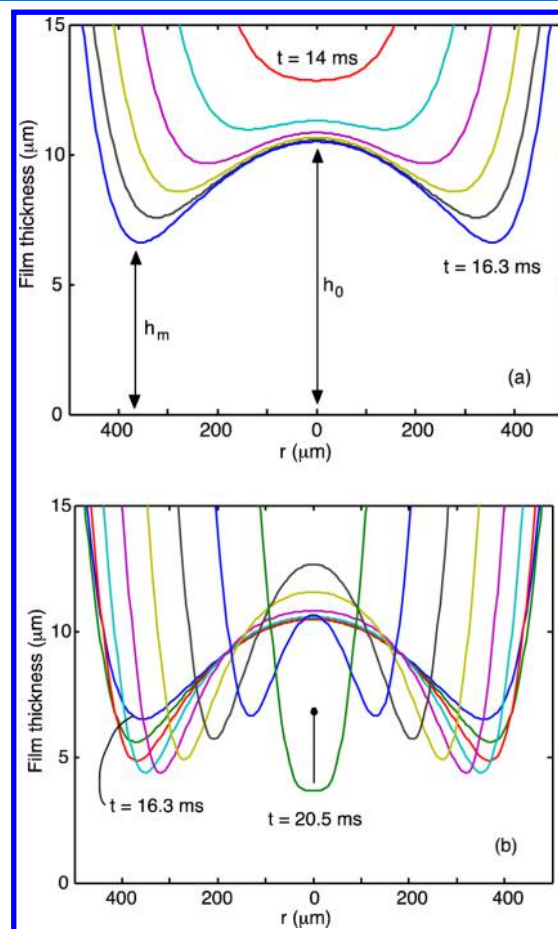


Figure 6. Thin film drainage during the first impact of the bubble from time 14 to 20.5 ms during (a) approach $t = 14$ –16.3 ms and (b) retraction $t = 16.3$ –20.5 ms. We define the thickness at the center h_o and minimum thickness h_m (both are functions of time).

the minimum film thickness occurs as a function of time. For this case of Teflon, experimental film rupture happened at 80 ms when the numerically predicted film thickness is approximately $1 \mu\text{m}$. Therefore, rupture is likely caused by the roughness of the Teflon, which can contain surface nanobubbles.

An interesting observation in Figure 5c is the sudden inward movement of the bubble surface at $t \approx 20$ ms (similar at $t \approx 40$ and 60 ms), that is, the moment the bubble departs from the surface, which also corresponds to the maximum negative velocity of Figure 5a and where the film force changes sign (becomes positive) in Figure 5b. During the pull-off phase, the film force generates a “suction effect”, which can be responsible for premature rupture of the film observed in coalescence of droplets.^{36,37}

In Figure 6 we show the film profile evolution during the first impact from time 14 to 20.5 ms of Figure 5. Figure 6a shows the bubble deformation during the approach phase where a curvature inversion appears, also known as “dimple”, that then grows. The minimum thickness h_m is no longer at the center. The occurrence of a dimple is a well-known phenomenon for

approaching deformable surfaces and was first observed experimentally many decades ago by Derjaguin and Kussakov³³ using interferometry and also more recently.^{3,34,35}

In Figure 6b we show the retracting phase. Even though the center of mass of the bubble is already moving away from the surface (negative velocity $V < 0$ in Figure 5a), the film is still thinning to about $4 \mu\text{m}$, which is not enough for film rupture, and the bubble bounces away from the surface. Note that bubble departure at $t = 20.5 \text{ ms}$ in Figure 6b corresponds to the maximum negative velocity in Figure 5a and the dip in the force in Figure 5b. Theoretically, subsequent bounces show very similar features of dimple formation happening at smaller separations. Unfortunately none of the experimental data of bouncing bubbles in clean water systems provide film thickness measurements to compare with the predictions given in Figure 6. On the other hand, comparison between a similar theory for bouncing bubbles in contaminated systems showed excellent agreement for the film drainage process.^{5,25,26} This provides us with the confidence that the currently predicted film heights are accurate from a spatiotemporal point of view.

■ SMALL BUBBLE RELEASED FAR FROM THE SURFACE

Now we move to bubbles impacting surfaces at terminal velocity. In Figure 7 we compare the model with experimental

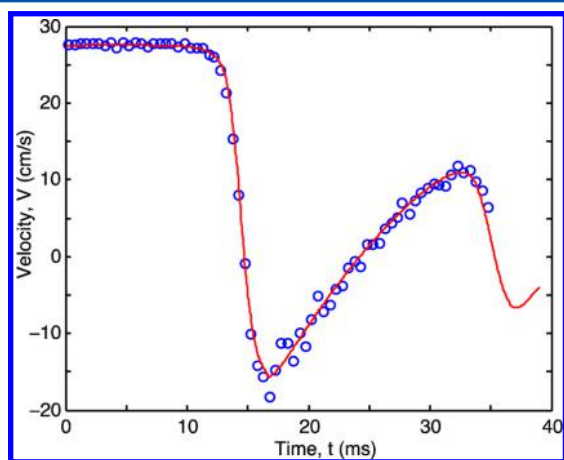


Figure 7. Comparison between theory (line) and experimental data of Zednikova et al.² (circles) for a bubble ($R = 0.525 \text{ mm}$) released far from the surface and impacting at terminal velocity $V_T = 27.5 \text{ cm/s}$. Theoretically, we take $r_m = 0.9R$ and $H_0 = 3.63 \text{ mm}$, and the aspect ratio of $\chi = 1.17$ given by eq 8 is kept constant for the calculation. No experimental data is available for $t > 35 \text{ ms}$.

data from Zednikova et al.² for a bubble with $R = 0.525 \text{ mm}$ that is rising at terminal velocity before impacting the surface. The aspect ratio during rise was calculated from eq 8 and resulted in $\chi = 1.17$, which is close to unity, so it was maintained at that value for the calculation even though after the first bounce the bubble becomes mostly spherical. General features of the system such as evolution of forces and film thickness at subsequent impacts are very similar to the case of large bubbles, so we will only show them in detail in the next section.

■ LARGE BUBBLE RELEASED FAR FROM THE SURFACE

For the case of a larger bubble ($R = 0.74 \text{ mm}$) impacting a smooth glass surface presented in Figure 8, the bubble rises with larger velocity ($V_T = 34.5 \text{ cm/s}$) and also larger deformation with an aspect ratio during rise of $\chi = 1.52$ according to eq 8. These features complicate the numerical procedure slightly. Numerically, we start the calculation with

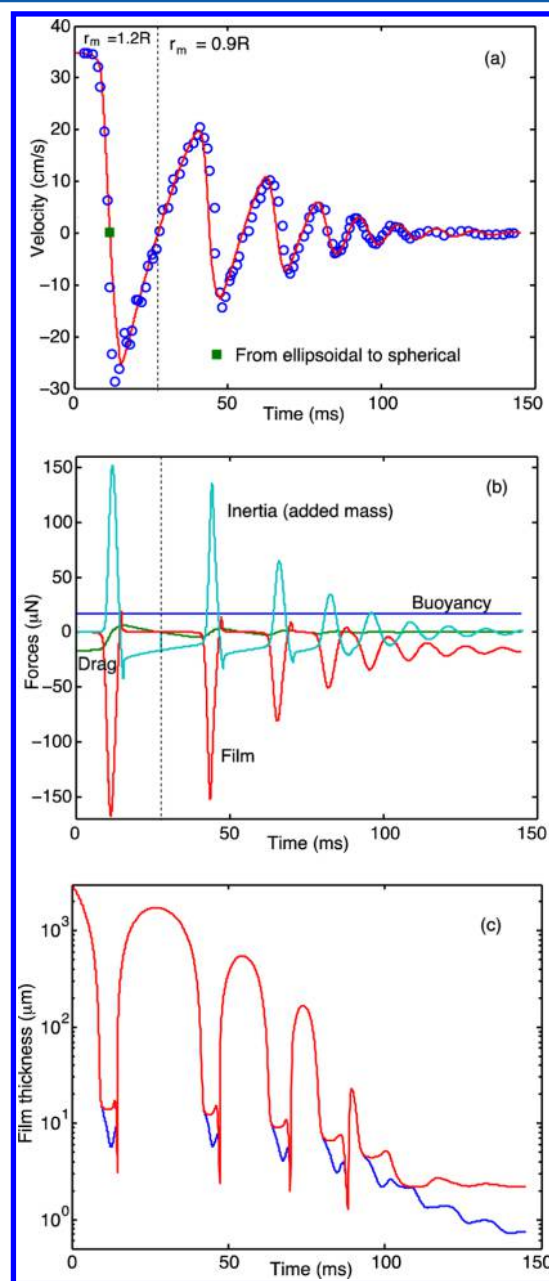


Figure 8. (a) Velocity as a function of time for a bubble ($R = 0.74 \text{ mm}$) impacting a glass surface corresponding to an experiment of Kosior et al.¹ (circles) compared with the model (line). Square symbol and vertical dotted line represent changes made to the parameters during numerical calculation. From $0 < t < 11.3 \text{ ms}$ we take an ellipsoidal bubble and after $t = 11.3 \text{ ms}$ spherical. Before the dashed line at $t = 25 \text{ ms}$ we take $r_m = 1.2R$ and after $r_m = 0.9R$. (b) Evolution of the forces. (c) Film heights h_0 and h_m as a function of time using log scale. Consecutive bounces appear to repeat each other at shorter separations.

the terminal velocity $V_T = 34.5$ cm/s as the initial velocity condition. Experimentally, during the rise process the bubble is deformed with an aspect ratio of $\chi = 1.52$, but after the first impact and subsequent impacts, the aspect ratio becomes close to $\chi = 1.0$ (a spherical bubble). Therefore, we decided to separate the time domain in three stages where we make the following changes: During the first stage a deformed bubble rises based on the analytical expression given by Moore²⁷ combined with the aspect ratio $\chi = 1.52$ and domain size $r_m = 1.2R$. In this case, we need to take r_m to be larger than the radius of the bubble R since the deformation during impact is about 0.6 mm (very close to R ; see also Figure 9). A further

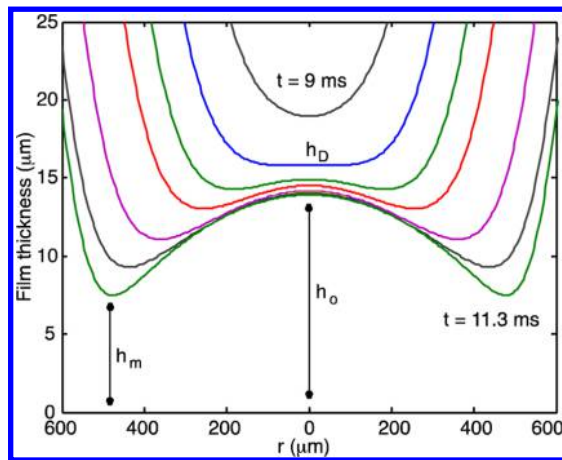


Figure 9. Film thickness during the first impact of the bubble ($R = 0.74$ mm) with $r_m = 1.2R$. We can see the extension of the maximum deformation that is around 0.6 mm. We define the dimple formation h_D , the height where the bubble surface first changes its curvature.

justification for this value is that for a deformed bubble with aspect ratio of $\chi = 1.52$, $r_m = 1.2R$ is roughly proportional to $r_m = 0.9R$ for an equivalent undeformed bubble. After the first impact (when the velocity becomes zero at $t = 11.3$ ms) we remove the deformation effect by changing χ from 1.54 to 1.0 (time marked by a square) and run the calculation until the velocity becomes zero again.

We continue the calculation after the first bounce at $t = 25$ ms by changing the domain size r_m from $1.2R$ to $0.9R$ (time marked by the dashed line). This is because the bubble becomes mostly spherical after the first impact, while it was considerably deformed during rise. The film force at this instant is zero. In the discussion we show a comparison where we maintain the domain size to be $r_m = 1.2R$. Unlike the Teflon case, where the experiment of Kosior et al.¹ showed premature film rupture, for the smooth glass case the experiment showed that the film remained much longer and rupture did not happen, presumably due to the presence of a repulsive surface force.

The evolution of forces presented in Figure 8b shows a very similar trend as Figure 5b. Note that at $t = 0$ the bubble is at its terminal velocity and the buoyancy force is exactly equal but opposite to the drag force. Toward the end (at $t = 150$ ms) buoyancy is compensated by the film force. In Figure 8c we show the film thickness during consecutive bounces. To show details of the bouncing process we show the position of the center h_o and rim h_m in a log scale. This allows visualization of multiple bounces of the bubble. The features repeat themselves at shorter separations until the bubble stops bouncing and only

film drainage is observed for $t > 100$ ms. Compared with Figure 5c we observe two extra bounces in this case.

In Figure 9 we plot the evolution of the film thickness during the first impact of the bubble with the glass surface where we show the extent of the deformation. The deformation of roughly 0.6 mm is comparable to the bubble radius $R = 0.74$ mm. A domain size $r_m = 0.9R$ would be too small to run the calculation, and the outer boundary of the film would interact with the deformation region and even can go through the surface. For that reason $r_m = 1.2R$ was chosen for the first impact consistent with the literature.⁶

DISCUSSION

The first occurrence of the dimple formation h_D can be predicted by an analytical expression³⁸ that was derived for a bubble with immobile boundary condition that impacts on a surface when approaching with constant velocity. The first moment of dimple formation h_D (See Figure 9) is given by $h_D = 0.4R\sqrt{2Ca}$ with $Ca = \mu V/\sigma$ being the capillary number. Here we need to adapt this result to account for the fact the bubble has a tangentially mobile boundary condition in which h_D can be written as

$$h_D = 0.4R\sqrt{Ca/2} \quad (19)$$

due to the factor of 4 difference in the drainage equation (eq 16) when compared to the immobile case. Dimple formation indicated in Figure 9 is $h_D \approx 15.5$ μm , in very good agreement with eq 19, which gives $h_D \approx 14.6$ μm .

The choice of the film drainage domain size r_m is important when capturing the physical features of the problem. Here we used $r_m = 0.9R$ for most of the calculations; the same value used before⁵ apart from the comparison in Figure 8a where we solved in two steps. For the large deformation we have taken $r_m = 1.2R$ and for the rest $r_m = 0.9R$. In Figure 10 we show the result if we keep $r_m = 1.2R$ for the entire calculation where we see agreement is still acceptable.

In Figure 10 we have also added the numerical simulations of Albadawi et al.⁸ using the volume of fluid method. Their solution is very good even though the terminal velocity is not captured exactly. Though expensive computationally when

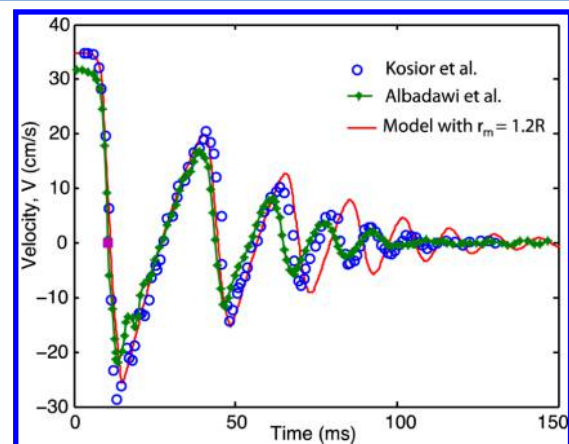


Figure 10. Using $r_m = 1.2R$ for the entire calculation of a bubble with $R = 0.74$ mm rising at constant velocity $V_T = 34.5$ cm/s against a glass surface compared to Kosior et al.¹ and with numerical solutions using the volume of fluid method.⁸ The square indicates the time when the bubble is changed from ellipsoidal ($\chi = 1.52$) to spherical ($\chi = 1.0$) when $V = 0$ for the first time.

compared to the force balance that only takes a few seconds to run, the full numerical simulation is able to capture details of the flow field and also the bubble shape oscillations after impact that are not captured in the force balance model.

CONCLUSION

The model based on a force balance captures the main physical features of a clean bubble during rise, impact, and bounce against a solid surface. For bubble rise in bulk where only buoyancy and drag forces play a role, we provided a fitting expression for the aspect ratio, which resulted in the correct terminal velocity using Moore's analytical formula. With the inclusion of added mass the force balance predicted the acceleration of a bubble starting from rest. The combination of lubrication theory for film drainage, deformation of the bubble, and force balance for the global movement proved robust when compared to experiments, predicting subsequent bounces of the bubble impacting against a solid surface. The model also provided film heights, which can be used as benchmark data for experiments when such data becomes available. This model can be extended to study oblique impact and bubble sliding along the solid surface.^{39,40} The force balance model could also be used in combination with full numerical simulations providing the bouncing behavior of bubbles that impact surfaces.

AUTHOR INFORMATION

Corresponding Author

*E-mail: manicar@ihpc.a-star.edu.sg.

Notes

The authors declare no competing financial interest.

ACKNOWLEDGMENTS

This work was supported in part by an Australian Research Council Discovery Project Grant to D.Y.C.C.

REFERENCES

- (1) Kosior, D.; Zawala, J.; Krasowska, M.; Malysa, K. Influence of n-octanol on the Bubble Impact Velocity, Bouncing and the Three Phase Contact Formation at Hydrophobic Solid Surfaces. *Colloids Surf. A: Physicochem. Eng. Aspects* **2014**, *441*, 788–795.
- (2) Fujasová-Zedníková, M.; Vobecká, L.; Vejrazka, J. Effect of Solid Material and Surfactant Presence on Interactions of Bubbles With Horizontal Solid Surface. *Can. J. Chem. Eng.* **2010**, *88*, 473–481.
- (3) Hendrix, M. H. W.; Manica, R.; Klaseboer, E.; Chan, D. Y. C.; Ohl, C.-D. Spatiotemporal Evolution of Thin Liquid Films during Impact of Water Bubbles on Glass on a Micrometer to Nanometer Scale. *Phys. Rev. Lett.* **2012**, *108*, 247803.
- (4) Tsao, H.-K.; Koch, D. L. Observations of High Reynolds Number Bubbles Interacting with a Rigid Wall. *Phys. Fluids* **1997**, *9*, 44–56.
- (5) Klaseboer, E.; Manica, R.; Hendrix, M. H. W.; Ohl, C.-D.; Chan, D. Y. C. A Force Balance Model for the Motion, Impact, and Bounce of Bubbles. *Phys. Fluids* **2014**, *26*, 092101.
- (6) Klaseboer, E.; Chevaillier, J.-Ph.; Maté, A.; Masbernat, O.; Gourdon, C. Model and Experiments of a Drop Impinging on an Immersed Wall. *Phys. Fluids* **2001**, *13*, 45–57.
- (7) Zenit, R.; Legendre, D. The Coefficient of Restitution for Air Bubbles Colliding against Solid Walls in Viscous Liquids. *Phys. Fluids* **2009**, *21*, 083306.
- (8) Albadawi, A.; Donoghue, D. B.; Robinson, A. J.; Murray, D. B.; Delauré, Y. M. C. On the Assessment of a VOF based Compressive Interface Capturing Scheme for the Analysis of Bubble Impact on and Bounce from a Flat Horizontal Surface. *Int. J. Multiphase Flow* **2014**, *65*, 82–97.
- (9) Brenner, H. The Slow Motion of a Sphere Through a Viscous Fluid towards a Plane Surface. *Chem. Eng. Sci.* **1961**, *16*, 242–251.
- (10) Bart, E. The Slow Unsteady Settling of a Fluid Sphere toward a Flat Fluid Interface. *Chem. Eng. Sci.* **1968**, *23*, 193–210.
- (11) Parkinson, L.; Ralston, J. Dynamic Aspects of Small Bubble and Hydrophilic Solid Encounters. *Adv. Colloid Interface Sci.* **2011**, *168*, 198–209.
- (12) Manica, R.; Parkinson, L.; Ralston, J.; Chan, D. Y. C. Interpreting the Dynamic Interaction between a Very Small Rising Bubble and a Hydrophilic Titania Surface. *J. Phys. Chem. C* **2010**, *114*, 1942–1946.
- (13) Zawala, J.; Malysa, K. Influence of the Impact Velocity and Size of the Film Formed on Bubble Coalescence Time at Water Surface. *Langmuir* **2011**, *27*, 2250–2257.
- (14) Suñol, F.; González-Cinca, R. Rise, Bouncing and Coalescence of Bubbles Impacting at a Free Surface. *Colloids Surf. A: Physicochem. Eng. Aspects* **2010**, *365*, 36–42.
- (15) Kelsall, G. H.; Tang, S.; Smith, A. L.; Yurdakul, S. Electrophoretic Behaviour of Bubbles in Aqueous Electrolytes. *Faraday Trans* **1996**, *92*, 3879–3893.
- (16) Bel Fdhila, R.; Duineveld, P. C. The Effect of Surfactant on the Rise of a Spherical Bubble at High Reynolds and Peclet Numbers. *Phys. Fluids* **1996**, *8*, 310–321.
- (17) Malysa, K.; Krasowska, M.; Krzan, M. Influence of Surface Active Substances on Bubble Motion and Collision with Various Interfaces. *Adv. Colloid Interface Sci.* **2005**, *114–115*, 205–225.
- (18) Duineveld, P. C. The Rise Velocity and Shape of Bubbles in Pure Water at High Reynolds Number. *J. Fluid Mech.* **1995**, *292*, 325–332.
- (19) Wu, M.; Gharib, M. Experimental Studies on the Shape and Path of Small Air Bubbles Rising in Clean Water. *Phys. Fluids* **2002**, *14*, 49–52.
- (20) Parkinson, L.; Sedev, R.; Fornasiero, D.; Ralston, J. The Terminal Rise Velocity of 10–100 mm Diameter Bubbles in Water. *J. Colloid Interface Sci.* **2008**, *322*, 168–172.
- (21) Clift, R.; Grace, J. R.; Weber, M. E. *Bubbles, Drops and Particles*; Academic Press: New York, 1978.
- (22) Chan, D. Y. C.; Klaseboer, E.; Manica, R. Film Drainage and Coalescence between Deformable Drops and Bubbles. *Soft Matter* **2010**, *7*, 2235–2264.
- (23) Chan, D. Y. C.; Klaseboer, E.; Manica, R. Theory of Non-equilibrium Force Measurements Involving Deformable Drops and Bubbles. *Adv. Colloid Interface Sci.* **2011**, *165*, 70–90.
- (24) Bretherton, F. P. The Motion of Long Bubbles in Tubes. *J. Fluid Mech.* **1961**, *10*, 166–188.
- (25) Manica, R.; Hendrix, M. H. W.; Klaseboer, E.; Ohl, C.-D.; Chan, D. Y. C. Effect of Film Hydrodynamic Boundary Condition on Bubble-Wall Impact. *Soft Matter* **2013**, *9*, 9755–9758.
- (26) Manica, R.; Hendrix, M. H. W.; Gupta, R.; Klaseboer, E.; Ohl, C.-D.; Chan, D. Y. C. Modelling Bubble Rise and Interaction with a Glass Surface. *Appl. Math. Model.* **2014**, *38*, 4249–4261.
- (27) Moore, D. W. The Velocity of Rise of Distorted Gas Bubbles in a Liquid of Small Viscosity. *J. Fluid Mech.* **1965**, *23*, 749–766.
- (28) Kharlamov, A. A.; Chára, Z.; Vlasák, P. Hydraulic Formulae for the Added Masses of an Impermeable Sphere Moving Near a Plane Wall. *J. Eng. Math.* **2007**, *62*, 161–172.
- (29) Mei, R.; Klausner, J. F.; Lawrence, C. J. A Note on the History Force on a Spherical Bubble at Finite Reynolds Number. *Phys. Fluids* **1994**, *6*, 418–420.
- (30) Legendre, D.; Zenit, R.; Velez-Cordero, J. R. On the Deformation of Gas Bubbles in Liquids. *Phys. Fluids* **2012**, *24*, 043303.
- (31) Schiller, L.; Naumann, A. Über die Grundlegenden Berechnungen bei der Schwerkraftaufbereitung. *Z. Ver. Dtsch. Ing.* **1933**, *77*, 318–320.
- (32) Miloh, T. Hydrodynamics of Deformable Contiguous Spherical Shapes in an Incompressible Inviscid Fluid. *J. Eng. Math.* **1977**, *11*, 349–372.
- (33) Derjaguin, B. V.; Kussakov, M. Anomalous Properties of Thin Polymolecular Films. *Acta Physicochim. URSS* **1939**, *10*, 26–45. Reprinted in *Prog. Surf. Sci.* **1992**, *40*, 26–45.

- (34) Fisher, L. R.; Hewitt, D.; Mitchell, E. E.; Ralston, J.; Wolfe, J. The Drainage of an Aqueous Film between a Solid Plane and an Air Bubble. *Adv. Colloid Interface Sci.* **1992**, *39*, 397–416.
- (35) Manica, R.; Connor, J. N.; Carnie, S. L.; Horn, R. G.; Chan, D. Y. C. Dynamics of Interactions Involving Deformable Drops: Hydrodynamic Dimpling Under Attractive and Repulsive Double-Layer Interactions. *Langmuir* **2007**, *23*, 626–637.
- (36) Gunes, D. Z.; Clain, X.; Breton, O.; Mayor, G.; Burbidge, A. S. Avalanches of Coalescence Events and Local Extensional Flows - Stabilisation or Destabilisation due to Surfactant. *J. Colloid Interface Sci.* **2010**, *343*, 79–86.
- (37) Bremond, N.; Thiam, A. R.; Bibette, J. Decompressing emulsion droplets favors coalescence. *Phys. Rev. Lett.* **2008**, *100*, 024501.
- (38) Klaseboer, E.; Manica, R.; Chan, D. Y. C. Universal behavior of the initial stage of drop impact. *Phys. Rev. Lett.* **2014**, *113*, 194501.
- (39) Del Castillo, L. A.; Ohnishi, S.; Horn, R. G. Inhibition of Bubble Coalescence: Effects of Salt Concentration and Speed of Approach. *J. Colloid Interface Sci.* **2011**, *356*, 316–324.
- (40) Del Castillo, L. A.; Ohnishi, S.; White, L. R.; Carnie, S. L.; Horn, R. G. Effect of Disjoining Pressure on Terminal Velocity of a Bubble Sliding Along an Inclined Wall. *J. Colloid Interface Sci.* **2011**, *364*, 505–511.